

# Detectability of Low-Level Broad-Band Signals Using Adaptive Matched-Field Processing with Vertical Aperture Arrays

Newell O. Booth, Ahmad T. Abawi, Phil W. Schey, and William S. Hodgkiss, *Member, IEEE*

**Abstract**—Alerted detection of low-level broad-band signals using adaptive matched-field processing (MFP) is illustrated in results from a shallow-water experiment carried out 12 km west of Point Loma, CA, in 200-m water of complex bathymetry. A 118-m vertical line array was deployed next to an identical line array tilted at 45 degrees. Array gain and signal excess for each of the arrays with linear and adaptive broad-band MFP is measured and compared using a low-level (118 dB//1  $\mu\text{Pa}^2/\text{Hz}$ ) broad-band signal from a towed source. Surface/submerged classification was achieved at the minimum detectable level due to the depth resolution obtained with MFP. The results are compared qualitatively with adaptive plane-wave beamforming on a horizontal line array deployed nearby.

**Index Terms**—Array performance, array processing, detection, matched-field processing.

## I. INTRODUCTION

ONE OF THE MOST challenging passive acoustic underwater detection issues is achieving a high probability of detection of low-level undersea sound sources in large shallow-water areas with cost-effective systems. Combinations of the following factors make the passive shallow-water acoustic detection problem particularly difficult to achieve with an affordable system.

- Sources of interest are usually extremely quiet.
- Littoral waters are typically cluttered with surface shipping interference, making both detection and classification difficult.
- Propagation in littoral waters is complex and lossy compared to the open ocean.
- Acoustic noise and propagation conditions vary temporally, spatially, and geographically.

This paper describes the potential of passive acoustic detection, classification, localization, and tracking at a minimum detectable signal-to-noise ratio (SNR) using arrays with both horizontal and vertical aperture and broad-band adaptive matched-field processing (MFP). Feasibility was demonstrated

using a towed source in a controlled shallow-water (200 m) experiment which was conducted in an area of moderately high shipping west of Point Loma near San Diego, CA. The experiment used vertical and tilted vertical arrays to demonstrate and measure:

- alerted detection of a towed broad-band acoustic source at frequencies up to 250 Hz at ranges to 4 km with input SNR approximately  $-20$  dB;
- localization and tracking in range, depth, and azimuth.

MFP is a generalization of beamforming where the propagation model for the energy arriving on an array of sensors is extended beyond plane and focused acoustic waves to include the multipath propagation occurring in ocean areas. It has been an active research area for the last 25 years since Bucker [8] formulated the approach where modeled and measured signals are correlated and a perfect match is measured by 0-dB correlation. MFP applications [13], [28], [32] localize sources of acoustic energy in range, depth, and bearing and require an accurate propagation model as well as knowledge of the array shape and the propagation parameters (sound speed profile, bathymetry, geoacoustic model). An overview of the development of MFP methods as applied to ocean acoustics, published by Baggeroer *et al.* in 1993 [3], summarizes the early experimental, modeling, and theoretical developments and describes the adaptive and linear processing approaches used in this paper. Additional historical perspective is provided by Ianniello [22].

Early work used high-level narrow-band source signals to determine the sensitivity of the MFP output and localization to the accuracy of the array shape and propagation parameters. The narrow-band results indicated that correlations between modeled and measured signals of better than  $-1$  dB were achievable, but that high sidelobe levels prevented unambiguous localization. Broad-band signals and frequency averaging were first suggested as a method of reducing the sidelobes by Baggeroer [2] in 1988. Simulations illustrating the improvement in peak to sidelobe ratio were published by Smith [29] in 1992. The first broad-band experimental results were reported by Westwood [31] that same year when he examined coherent and incoherent frequency combination methods in deep water for broad-band (55–95 Hz) signals. The results illustrated an improvement in the peak-to-sidelobe ratio for most combination methods. Other more recent experiments [7], [23] in different areas with multitone and broad-band signals demonstrated that signal bandwidth reduces sidelobe ambiguities obtaining unambiguous source tracks.

Manuscript received August 15, 1998; revised May 19, 2000. This work was supported by Dr. John Tague, Office of Naval Research, Code 321-US, under Project RJ35K85, Environmentally Enhanced Array Processing.

N. O. Booth, A. T. Abawi and P. W. Schey are with the Acoustics Branch, Code D857, Space and Naval Warfare (SPAWAR) Systems Center, San Diego, CA 92152-5000 USA.

W. S. Hodgkiss is with the Marine Physical Laboratory, Scripps Institution of Oceanography, University of California at San Diego, La Jolla, CA 92093-0701 USA.

Publisher Item Identifier S 0364-9059(00)06640-1.

TABLE I  
TABLE OF ABBREVIATIONS

$\alpha$	Array tilt	$N_t$	Number of FFTs / epoch
$AG$	Array Gain	$N_s$	FFT length
$ANG$	Array Noise Gain	$N(f)$	Number of independent samples
AODS	All Optical Deployable System	$OSNR$	Output Signal-to-Noise Ratio
AODS-N	Northern AODS array	$P_d$	Probability of detection
$ASGD$	Array Signal Gain Degradation	$P_{fa}$	Probability of false alarm
BB1, BB2	Broadband source signal names	$P_o$	Output power
$BDL$	Bearing Detection Level	$P_n$	Element average noise power
BTR	Bearing-Time Record	$P_{s+n}$	Element average signal plus noise power
$C$	Correlation	PWB	Plane Wave Beamforming
CSM	Cross-Spectral Matrix	$\mathbf{r}$	Search vector (range, bearing, depth)
COPSL	Cell Output Power Spectrum Level	$r_s$	Apparent Source Range
$d$	detection index	$r_s$	True source range
$d_a$	Water depth at array	$RDL$	Range Detection Level
$d_s$	Water depth at source	$RSL$	Received Signal Level
$DI$	Directivity Index	RTR	Range-Time Record
$DT$	Detection Threshold	$\mathbf{s}$	Steering vector
$\mathbf{g}$	Modeled replica vector	$SE$	Signal Excess
$G$	Processor gain	$SNR$	Signal-to-Noise Ratio
HLA	Horizontal Line Array	$T_s$	FFT duration
$INL$	Input Noise Level	$T_e$	Epoch duration
$IRSL$	Input Received Spectral Level	TLA	Tilted Line Array
$IRSSL$	Input Received Signal Spectral Level	VLA	Vertical Line Array
$ISNR$	Input Signal-to-Noise Ratio	$\mathbf{w}_L$	Weight vector for linear processor
$\mathbf{K}$	Cross-Spectral Matrix	$\mathbf{w}_{MVDR}$	Weight vector for MVDR processor
$L$	Array length	$W$	Processing bandwidth
MFP	Matched-Field Processing	$W_s$	FFT binwidth
$ML_x$	Marking Level of display for x%	$WNG$	White Noise Gain
MVDR	Minimum Variance Distortionless Response	$\mathbf{x}$	Data vector
$NL$	Noise Level	$z_s$	Apparent source depth
$N_e$	Number of array elements	$z_s$	True source depth

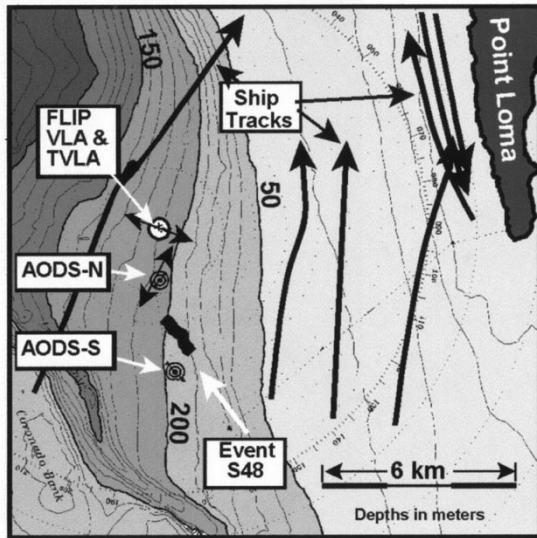
The application of MFP to detection and localization involves searching in range, depth, and bearing while assuming the array shape and propagation parameters are known. Sidelobe reduction is very important in the detection problem to prevent the sidelobe energy of loud interfering surface ships from masking the signal of most interest which is several orders of magnitude quieter than the interferer. Sidelobe effects are additionally mitigated by using adaptive MFP [3], [6], [12], [25] which minimizes the beamformer energy subject to the constraint that a signal that matches the modeled steering vector is passed without loss.

The objective of this paper is to present experimental results which demonstrate the feasibility of achieving detection and localization of low-level submerged acoustic sources in shallow water. Development issues such as unalerted search, array element localization, environmental measurement, and operator loading have been postponed to focus on the goal of determining if the performance improvement obtained is sufficient to warrant the investment required to solve them.

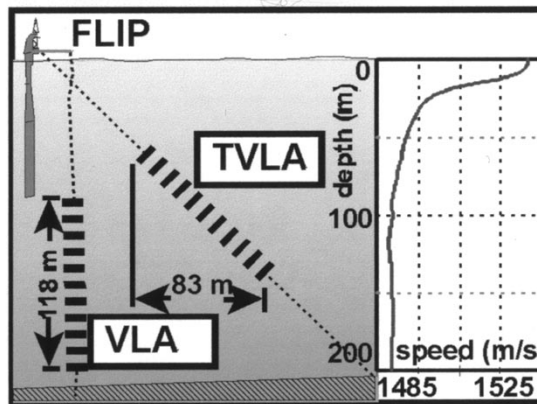
The SWellEx-96 experiment and the processing methods are described in the next two sections. The potential of adaptive MFP is then illustrated using a tilted line array (TLA) with

adaptive MFP. This array and processing combination resulted in the largest signal excess for the low-level signal. After introducing range-time and bearing-time record display formats, the noise directionality in the range, depth, and bearing search space is described. The local SNR, estimated by filtering of the range-time and bearing-time records, is used as a detection statistic to obtain a display that illustrates the detection of weak signals. Classification of the source as submerged is illustrated by examining range-time records which are focused at different depths. A track cell spectrogram is also generated by focusing on the source track as it moves in range, depth, and bearing.

The array and processing comparisons section compares the detection performance of the co-located tilted and vertical arrays with both linear and adaptive processing. Qualitative comparisons of the MFP results with the traditional plane-wave beamforming (PWB) approach using a horizontal line array (HLA) are also presented. The last technical section defines quantitative measures of MFP detection performance presenting estimates of array gain, detection threshold, and signal excess achieved for the various arrays and MFP methods evaluated. Table I lists the abbreviations used.



(a)



(b)

Fig. 1. (a) SWellEx-96 experiment site showing the FLIP and AODS arrays. The source track and surface shipping tracks for the 1 h of event S48 are also shown. (b) The VLA and TVLA are shown to scale as deployed from FLIP. A typical sound speed profile is also shown.

## II. SWELLEX-96 EXPERIMENT

The SWellEx-96 experiment was conducted between May 10 and 18, 1996, approximately 12 km from the tip of Point Loma near San Diego, CA [1], [7]. The location, bathymetry, and sound speed profile of the site are shown in Fig. 1. The acoustic sensors deployed in SWellEx-96 included:

- a vertical line array (VLA) and a tilted line array (TLA), deployed by the Floating Instrument Platform (R/P FLIP);
- the All Optical Deployable System (AODS) consisting of two HLA's installed on the sea floor; the northern AODS array was designated AODS-N while the southern array, AODS-S, was not used in this analysis.

The MFP results reported in this paper were obtained from the VLA and TLA arrays deployed from R/P FLIP at the position shown in Fig. 1(a). Each of these arrays [20] consisted of 64 calibrated hydrophone elements, equally spaced at 1.875 m over a 118.1-m aperture and sampled at 1500 Hz. The arrays were deployed in the configuration shown in Fig. 1(b) with the TLA tilted toward FLIP at an angle of  $\sim 45^\circ$  and a heading

TABLE II  
EVENT S48 SOURCE SIGNALS, 12 MAY, 1996, 2245–2345

Time min	Signal Name	Description
0-5	9-Tone Comb	155dB//mPa <sup>2</sup> , 9 tones 112-388 Hz
5-15	Broadband (BB1)	$\sim 142\text{dB//mPa}^2/\text{Hz}$ , 100-400 Hz
15-25	BB2	BB1 - 12 dB, 100-400 Hz
25-35	BB3	BB1 - 16 dB, 100-400 Hz
35-40	BB4	BB1 - 20 dB, 100-400 Hz
40-55	BB5	BB1 - 24 dB, 100-400 Hz
55-60	9-Tone Comb	155dB//mPa <sup>2</sup> , 9 tones 112-388 Hz

of  $111^\circ$  relative to true north. Processing results from the TLA used every third element forming a 22-element subarray with a spacing of 5.625 m. Results from the VLA used a similar subarray with 21 elements. The 15th element from the array bottom was omitted because it was not functional. The water depth at FLIP was 216 m. A sound speed profile taken the day of the event is also shown in Fig. 1(b).

The PWB results reported in this paper were obtained from the AODS-N HLA deployed  $\sim 1.5$  km south of FLIP. The data analysis used 28 elements, sampled at 3277 Hz, spread aperiodically over a 240-m horizontal aperture. The array was slightly curved with a 15-m total displacement from a straight line.

Fig. 1(a) also shows the tracks of surface ships during event S48. The tracks were obtained from a video recording of the radar mounted on FLIP.

A J15-3 acoustic source, towed from the R/V Sproul, transmitted various broad-band and multitone signals at frequencies between 50 and 400 Hz. For the results reported in this paper, R/V Sproul drifted in a quiet mode with the source deployed at a 56-m depth over the track labeled event S48 in Fig. 1(a). The range varied between 4 and 5 km from the FLIP arrays and between 2 and 3 km from the AODS-N array. Event S48 was conducted on May 12, 1996, between 2245 and 2345 GMT.

During this 1-h event, the source transmitted the series of signals shown in Table II. During the first and last 5 min of the 1-h period, the source transmitted nine high-level narrow-band tones which were used to measure array signal gain. A 100–400-Hz broad-band signal was transmitted at a decreasing source level between the narrow-band transmissions. During the 5-15-min period, the broad-band signal was transmitted at high level ( $\sim 142\text{ dB//}\mu\text{Pa}^2/\text{Hz}$ ) to allow accurate measurement of the received level and spectrum. This time period is called signal BB1. The same broad-band signal was attenuated by  $-12$ ,  $-16$ ,  $-20$ , and  $-24$  dB to generate signals BB2 through BB5 for the time periods listed in Table II.

The element-averaged TLA spectrogram is shown in Fig. 2 where only the highest level (BB1) signal is seen. The horizontal white lines indicate the times when the lowest level signal, labeled BB5, was transmitted. The subject of this paper is the detection, localization, and measurement of the signal excess obtained with these low-level broad-band signals on the arrays.

## III. PROCESSING METHODS AND PARAMETERS

This section describes both linear and adaptive matched-field and plane-wave processing methods which are used on various

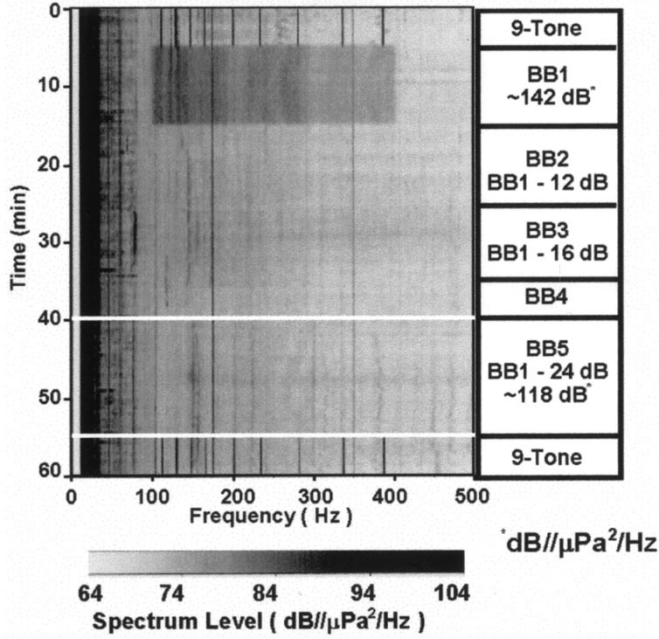


Fig. 2. Event S48 spectrogram obtained by averaging individual spectrograms for the 22 elements used in processing the TLA. The median level of the entire gram is 74 dB// $\mu\text{Pa}^2/\text{Hz}$ . The table at the far right summarizes the signals transmitted during the event. The signals are described in more detail in Table II.

arrays in this paper. The linear processor is fundamentally an unshaded frequency-domain beamformer. The adaptive processor, also implemented in the frequency domain, adjusts the beamformer weights to minimize the contribution of interfering signals to the beam output, subject to the constraint of maintaining the response for signals that match the steering vector. Both processors can be implemented with plane-wave or matched-field steering vectors. The plane-wave beamformer calculates steering vectors for an angular search space using a plane-wave (or focused plane-wave) model for the signal arrivals. The matched-field processor differs in that the steering vectors are calculated in a search space  $\mathbf{r}$  of range, depth, and azimuth using a propagation model that accounts for the complex multipath structure present in the acoustic field. Matched-field steering vectors are often called replicas or replica vectors.

The frequency-domain processing approach is described in Section III-A followed by a description of the means of calculating the linear and adaptive processing weight vectors. The modeling approach used in calculating the replica vectors is described in Section III-C. Section III-D describes the processing parameters chosen and discusses the issues involved in the choice of the parameters.

#### A. Narrow-Band and Broad-Band Processing

Each  $T_s$  seconds of data from  $N_e$  elements was Fourier analyzed with a Kaiser–Bessel window [19] with 50% overlap to form a  $N_e$ -element data vector  $\mathbf{x}(f_k, t_j)$  for each frequency  $f_k$  and time  $t_j$ . The cross-spectral matrix (CSM)  $\mathbf{K}(f_k, t)$  was esti-

mated [5], [18] by averaging  $N_t$  outer products of the data vectors for the duration of an epoch  $T_e = (N_t + 1/2)T_s$

$$\mathbf{K}(f_k, t) = \frac{1}{N_t} \sum_{j=1}^{N_t} \mathbf{x}(f_k, t_j) \mathbf{x}^*(f_k, t_j) \quad (1)$$

where  $*$  indicates complex-conjugate transpose. The specific processing parameters for the various arrays are listed in Table V in the last part of this section along with a discussion of the issues involved in the choice of the duration of the fast Fourier transform (FFT) and the epoch.

For each position in the search space  $\mathbf{r}$ , the processor estimates the normalized cross correlation of the received data with weight vectors  $\mathbf{w}$ . For each time  $t$  and frequency  $f_k$ , the narrow-band correlation was calculated using

$$C(f_k, \mathbf{r}, \alpha, t) = \frac{\mathbf{w}^*(f_k, \mathbf{r}, \alpha) \mathbf{K}(f_k, t) \mathbf{w}(f_k, \mathbf{r}, \alpha)}{\frac{1}{N_e} \text{Tr}(\mathbf{K}(f_k, t))} \quad (2)$$

where the trace of the CSM is given by

$$\begin{aligned} \text{Tr}(\mathbf{K}(f_k, t)) &= \sum_{l=1}^{N_e} \frac{1}{N_t} \sum_{j=1}^{N_t} \mathbf{x}_l(f_k, t_j) \mathbf{x}_l^*(f_k, t_j) \\ &= N_e \cdot \bar{P}_{s+n}(f_k, t). \end{aligned} \quad (3)$$

$\bar{P}_{s+n}(f_k, t)$  is the input signal-plus-noise power averaged over the elements and over the epoch. The correlation is then the output power

$$P_o(f_k, \mathbf{r}, t) = \mathbf{w}^*(f_k, \mathbf{r}, t) \mathbf{K}(f_k, t) \mathbf{w}(f_k, \mathbf{r}, t) \quad (4)$$

normalized by the element average input signal-plus-noise power

$$C(f_k, \mathbf{r}, \alpha, t) = \frac{P_o(f_k, \mathbf{r}, t)}{\bar{P}_{s+n}(f_k, t)}. \quad (5)$$

The frequency combination process which maximizes the output SNR for any wide-bandwidth signal with known power spectral density ( $P_s(f_k)$ ) in a noise background with noise power spectral density ( $P_n(f_k)$ ) is an Eckart filter [9, p. 376], [15]. The output  $O_E$  is given by

$$O_E \propto \sum_{f_k} \left( \frac{\mathbf{w}^*(f_k) \mathbf{K}(f_k) \mathbf{w}(f_k)}{P_n(f_k)} \cdot \frac{P_s(f_k)}{P_n(f_k)} \right). \quad (6)$$

While the detailed shape of the source power spectral density  $P_s(f_k)$  is not necessarily known, it is known that both ship and oceanic noise typically decrease with increasing frequency [9, p. 344]. For the purposes of this paper, we assume that the signal-to-noise spectrum is independent of frequency over the band of interest

$$\frac{P_s(f_k)}{P_n(f_k)} = \xi \quad (7)$$

obtaining

$$O \propto \sum_{f_k} \left( \frac{\mathbf{w}^*(f_k) \mathbf{K}(f_k) \mathbf{w}(f_k)}{P_n(f_k)} \right). \quad (8)$$

In addition, since detection systems are optimized for low SNR targets, we assume that  $\xi \ll 1$  and put  $\overline{P_{s+n}}(f_k) = P_n(f_k)$  in (5). Under these assumptions and using (4), we obtain a processor with an output proportional to the frequency-averaged correlation

$$O \propto \sum_{f_k} C(f_k). \quad (9)$$

The broad-band output presented in this paper is the processor described above and was obtained by incoherently averaging the correlation estimate over  $N_f$  frequencies

$$\overline{C(\mathbf{r}, \alpha, t)} = \frac{1}{N_f} \sum_{k=1}^{N_f} C(f_k, \mathbf{r}, \alpha, t). \quad (10)$$

The frequency-averaged correlation has the following additional physical interpretations.

- When focused on a source with a high input SNR ( $\mathbf{r} = \mathbf{r}_s$  and  $\text{Tr}(\mathbf{K}(f)) \approx N_e \cdot P_s(f)$ ), correlation averaging normalizes for signal amplitude variation over frequency providing a result that is the frequency average correlation between the measured CSM and the weight vector. The frequency-averaged array signal gain degradation (ASGD) is given by [7]

$$\text{ASGD} = 10 \log \left( \frac{1}{N_f} \sum_{k=1}^{N_f} \frac{P_o(f_k, \mathbf{r}_s)}{\overline{P_s}(f_k)} \right) = 10 \log(\overline{C(\mathbf{r}_s)}), \quad (11)$$

ASGD was estimated before and after the broad-band signals were transmitted using linear MFP and averaging only the bins with high level tones.

- When focused where no source signal exists ( $\mathbf{r} = \mathbf{r}_o$  and  $\text{Tr}(\mathbf{K}(f)) \approx N_e \cdot \overline{P_n}(f_k)$ ), the output is an estimate of the frequency averaged array noise gain (ANG)

$$\text{ANG} = 10 \log \left( \frac{1}{N_f} \sum_{k=1}^{N_f} \frac{P_{bn}(f_k, \mathbf{r}_o)}{\overline{P_n}(f_k)} \right) = 10 \log(\overline{C(\mathbf{r}_o)}) \quad (12)$$

where  $P_{bn}(f_k)$  is the beam noise power spectrum and  $\overline{P_n}(f_k)$  is the element average noise power spectrum. This interpretation should be used with caution because the estimate of ANG is biased low because of insufficient cross-spectral averaging (see (22) at the end of this section).

This process differs from the frequency averaging of broad-band sources first suggested by Baggeroer, Kuperman, and Schmidt [2] as a means of reinforcing the main lobe and averaging out the sidelobes. They arrived at the method of averaging beam power levels in decibels by trial and error. The method used here is similar to that used in simulations by Smith, Feuillade, and DelBalzo [29]. Westwood [31] examined several different methods of summing over frequency and over elements, including the method described in (10). His preference for high SNR data in deep water was to include only the off-diagonal elements of the product of the modeled and data CSM's in the beam output frequency average. We

chose the method in (2) and (10) because the results appeared to be the same or better than those achieved using Westwood's methods when applied to our data. We also wished to use the physical interpretation described above for understanding and comparing the results of different arrays and processing methods.

### B. Adaptive and Linear Weight Vectors

The weight vectors  $\mathbf{w}(f_k, \mathbf{r}, \alpha)$  are calculated for each position in the search space defined by the source position  $\mathbf{r}$  (range, depth, and azimuth) and array tilt ( $\alpha$ ) for matched-field replicas. The search space reduces to range and azimuth for focused plane-wave replicas and azimuth only for plane-wave replicas.

The weight vectors for the standard linear processor (also called a Bartlett processor) are the steering vectors  $\mathbf{s}$  defined in the next section, normalized by the number of elements,

$$\mathbf{w}_L = \frac{\mathbf{s}}{N_e}. \quad (13)$$

The adaptive process used in the analysis is the minimum variance distortionless response [3] (MVDR) with white noise constraint [12], [17]. It differs from the linear processor in that the adaptive weight vectors  $\mathbf{w}_A$  for each epoch are calculated using the CSM which was measured during that epoch

$$\mathbf{w}_A = \frac{(\mathbf{K} + \varepsilon \mathbf{I})^{-1} \mathbf{s}}{\mathbf{s}^* (\mathbf{K} + \varepsilon \mathbf{I})^{-1} \mathbf{s}} \quad (14)$$

where  $\mathbf{I}$  is the identity matrix and  $\varepsilon$  is the white noise added to ensure that  $\mathbf{K} + \varepsilon \mathbf{I}$  can be inverted and/or to reduce signal gain degradation from replica mismatch at a high SNR.

The white noise gain constraint was used as a means of choosing the value of  $\varepsilon$ . The array gain for a processor and array in a signal field consisting of a perfectly matched signal and spatially white noise ( $\mathbf{K}_w = P_s \mathbf{s} \mathbf{s}^* + P_n \mathbf{I}$ ) is given by the inverse of the magnitude squared of the weight vectors [12]. For the adaptive processor, it is given by

$$G_w(\varepsilon) = (\mathbf{w}_A^* \mathbf{w}_A)^{-1}. \quad (15)$$

For each steering vector, frequency, and CSM, the added white noise ( $\varepsilon$ ) is iteratively increased [17] until the white noise gain satisfies  $\delta^2 < G_w < N_e$ , where  $\delta^2$  is a variable chosen to provide a balance between interference rejection and mismatch loss. When  $\delta^2$  is small ( $|\mathbf{w}_A|$  is large), the processor behaves like a purely adaptive processor ( $\varepsilon = 0$ ). When  $\delta^2 = N_e$ , the processor behaves like a linear processor. The white noise gain value is described according to

$$\text{WNG} = 10 \log \left( \frac{\delta^2}{N_e} \right) \leq 0 \text{ dB} \quad (16)$$

where  $\text{WNG} = 0$  dB corresponds to a linear processor and  $\text{WNG} = -\infty$  dB corresponds to a pure MVDR processor.

$\text{WNG} = -3$  dB was used in all of the MVDR results shown in this paper. This was chosen empirically as a compromise between the robustness of a linear processor and the interference rejection of the pure MVDR processor.

TABLE III  
GEOACOUSTIC MODEL. LINEAR PROFILE IN EACH LAYER

$z$ (m)	$c_c$ (m/s)	$\rho$ (g/cm <sup>3</sup> )	$\alpha_c$ (dB/km/Hz)	Bottom Type
198	1574	1.76	0.22	sediment
228	1595	1.76	0.24	
228	1691	2.06	0.02	mudstone
1028	3056	2.06	0.02	
1028	5200	2.66	0.02	basement

$z$ : depth from the surface;  $c_c$ : compressional sound speed;  $\rho$ : density;  $\alpha_c$ : compressional wave attenuation. The geoacoustic model assumed no shear waves.

### C. Replica Calculation

The steering vectors  $\mathbf{s}(f_k, \mathbf{r}, \alpha)$  are given by

$$\mathbf{s} = \frac{\mathbf{g}\sqrt{N_e}}{|\mathbf{g}|}. \quad (17)$$

The modeled replica fields  $\mathbf{g}(f_k, \mathbf{r}, \alpha)$  were calculated for each assumed source position  $\mathbf{r}$  and array tilt  $\alpha$  using the KRAKEN normal mode model [26]. The sound velocity profile, shown in Fig. 1(b), was measured during the previous 24 h and within a 5-km range of arrays. The geoacoustic model (Table III) for propagation in the bottom was from historical data [1] which were refined by geoacoustic inversions from an earlier experiment [4]. Independent array element location arrival time measurements were made during the events but were not used in this analysis. Instead, the array was assumed to be straight and the array tilt was included in the search parameters. For all TLA results reported here, one tilt ( $\alpha = 47^\circ$ ) was used. It was obtained as  $\alpha_{\max}$  for the maximum correlation  $\overline{C}(\mathbf{r}, \alpha, t)$  averaged over the pilot tones at the beginning of the event. The same answer was obtained for the maximum pilot frequency-averaged correlation at the end of the event, indicating that the array did not change tilt during the event. Previous experiments using more parameters in the array shape model have shown good agreement with the independent measurements [21].

Note from Fig. 1(a) that the water depth at the position of the source is less than the depth at the receiving arrays resulting in down and across slope propagation from the source to the array. The KRAKEN model used in the replica calculations is range-independent. The water depth was assumed to be the depth at the position of the receiving array. The assumption of range-independent propagation causes errors in the range and depth estimate of the localization peak with small mismatch loss for processing bandwidths greater than 1 octave. D'Spain [14] recently published a full description and explanation of these errors. The phenomenon was predicted and measured under downward refracting adiabatic propagation conditions. The following properties were used in this work to obtain detection and localization.

- Significant mismatch in bathymetry (factor  $\leq 2$ ) between data and calculated replicas in downward refracting shallow water with adiabatic propagation causes an error in the range and depth estimate obtained with MFP. The loss in signal gain due to the depth mismatch is small ( $\leq 1$  dB). As a result, a source can be successfully detected but at the incorrect range and depth.

TABLE IV  
FREQUENCY AVERAGE ASG DEGRADATION MEASUREMENTS (112, 130, 148, 166, AND 201 Hz TONES, LINEAR PROCESSING)

Time Period	0 - 5 min	55 - 60 min
Median ASGD (dB)	$-0.9 \pm 0.1$	$-1.4 \pm 0.2$
Source Range (km)	3.7	5.05
SNR (dB)	$>15$	$>15$

- The apparent source depth  $\hat{z}_s$  is given by

$$\hat{z}_s = \frac{d_a}{d_s z_s} \quad (18)$$

where  $z_s$  is the true source depth,  $d_s$  is the water depth at the location of the source, and  $d_a$  is the water depth at the position of the array. This simple relationship results from mode stretching as the signal propagates to deeper water.

- The apparent source range  $\hat{r}_s$  is given by

$$\hat{r}_s = d_a^2 \int_0^{r_s} \frac{1}{d(r)^2} dr \quad (19)$$

where  $r_s$  is the true range to the source and  $d(r)$  is the range-dependent water depth along the propagation path between the source and the array. For the nearly linear slope for the propagation path, we assume

$$d(r) = d_a + \frac{(d_s - d_a)}{r_s} r \quad (20)$$

obtaining

$$\hat{r}_s = \frac{d_a}{d_s} r_s. \quad (21)$$

After the source is detected, the correct range and depth can be calculated from (18) and (21).

The quality of the replicas was measured before and after the broad-band signals were transmitted by estimating ASGD with linear processing using (11). Only the frequency bins with high-level signals in the band of the processing (112, 130, 148, 166 and 201 Hz) were included in the average. The results are summarized in Table IV.

The peak-to-sidelobe ratio obtained with linear MFP on the high-level signals is a measure of MFP performance of an array in an ocean environment [7]. For the TLA in the SWellEX-96 experiment, the peak sidelobe in the frequency-averaged range–depth search space at the bearing of the source ( $0 < \text{range} < 10$  km,  $0 < \text{depth} < 200$  m) was  $-4$  dB. With the  $-1$ -dB degradation, the resulting peak-to-sidelobe ratio was approximately 3 dB.

### D. Processing Parameters

The characteristics and processing parameters for the arrays are summarized in Table V.

The FFT bandwidth  $W_s$  and the epoch duration  $T_e$  used to obtain the cross-spectral matrices were chosen empirically with an emphasis on minimizing mismatch loss. CSM estimation has

TABLE V  
ARRAY AND PROCESSING PARAMETERS

Parameter	Symbol (units)	TLA	VLA	AODS-N
Sampling Rate	$f$ (Hz)	1,500	1,500	3,276.8
FFT Length	$N_s$ (samples)	2,048	2,048	4,096
FFT Duration	$T_s$ (s)	1.37	1.37	1.25
FFT Binwidth *	$W_s = 1.65 / T_s$ (Hz)	1.2	1.2	1.32
* Kaiser-Bessel $\alpha = 2.5$ , 50% overlap				
Epoch Duration	$T_e$ (s)	30.14	30.14	30
No. 50% FFTs /Epoch	$N_T$	43	43	47
Processing Band	$W$ (Hz)	100-250	100-250	100-250
No. of Elements	$N_e$	22	21	28
Time-Bandwidth Product	$TW$	4,521	4,521	4,500
Water Depth	$d_a$ (m)	216	216	213
Array Length	$L$ (m)	118	118	240
Vertical Aperture	(m)	83	118	< 3
Horizontal Aperture	(m)	83	< 5	240 by 15
Endfire Heading	(° // North)	111	N/A	36
Range Resolution	(m) @ 250 Hz	200	150	N/A
Range Sampling	(m)	25	25	N/A
Depth Resolution	(m) @ 250 Hz	15	15	N/A
Bearing Resolution	(°) @ 250 Hz	4	N/A	1.4
Bearing Sampling	(°)	25	N/A	25

been examined for plane-wave adaptive beamformers by Grant [18]. Several of his results are applicable when interpreted in the context of MFP.

A wide-binwidth short FFT duration is desirable to minimize the number of frequencies in the frequency average (10) and to maximize the number of samples averaged in each epoch  $T_e$  to obtain the CSM (1). However, two phenomena limit the binwidth.

- The duration of the FFT must be longer than the time required for a signal to traverse the largest aperture of the array. For the arrays in this study, the resulting binwidth must be less than 6 Hz. For vertical arrays where most of the important signal and noise propagation is broadside to the array, the binwidth may be increased.
- The binwidth must be less than the bandwidth of the applicability of the steering vectors  $\mathbf{s}$  [see (17)], which is determined by loss of array signal gain between a signal at one frequency and a replica at another frequency. Prior to completing the processing, we verified that no measurable ASGD from frequency mismatch within an FFT binwidth occurred for signals within the processing band  $W$  and at the search ranges used in the experiment.

A long epoch duration is desirable to: 1) minimize the rate of beamforming calculations and 2) to maximize the number of samples averaged in the CSM. However, the CSM averaging time is limited by the stationarity of the signal and noise cross-spectral matrices and statistical requirements for estimating the CSM's.

- The maximum CSM integration time should be less than the time required for a typical low-level source to traverse a search cell. This time is large for distant sources seen by arrays using plane-wave beamforming. MFP in the SWelIEX-96 environment, however, has a

resolution in range of approximately 200 m [7]. A 13-kn source (target or interference) traveling radially to the array will transverse this range cell in the 30-s epoch duration. Faster interferences will be in several resolution cells during the integration, resulting in less effective adaptive beamforming. A faster target will suffer a loss in array signal gain because the steering vector for a cell will be valid only for the time that the source is within the search cell. However, faster targets will have higher source spectral levels reducing the need for signal gain.

- The theory of CSM estimation was first described by Capon [10], [11]. Its role in adaptive plane-wave beamforming was the subject of Grant's paper [18]. The important result is that the beam noise level is underestimated resulting in a measured ANG ( $ANG_M$ ) that is related to the true ANG ( $ANG_T$ ) by

$$ANG_M = ANG_T + 10 \log \frac{N_T - N_e + 1}{N_T} \quad (22)$$

where  $N_T$  is the number of independent samples in the CSM and  $N_e$  is the number of elements. In this analysis with a 50% overlapped Kaiser-Bessel window ( $N_T \approx 2N_e$ ), the estimation error is approximately  $-3$  dB. The estimation error does not affect SNR or array gain measurements since the estimation error applies equally to both the broad-band signal and the noise.

#### IV. DETECTION USING A TLA WITH ADAPTIVE MFP

The results obtained during event S48 using 22 elements of the TLA receiver deployed from FLIP (Fig. 1) are presented in this section. They illustrate the full potential of MFP to provide array gain in addition to range, depth, and azimuth resolution

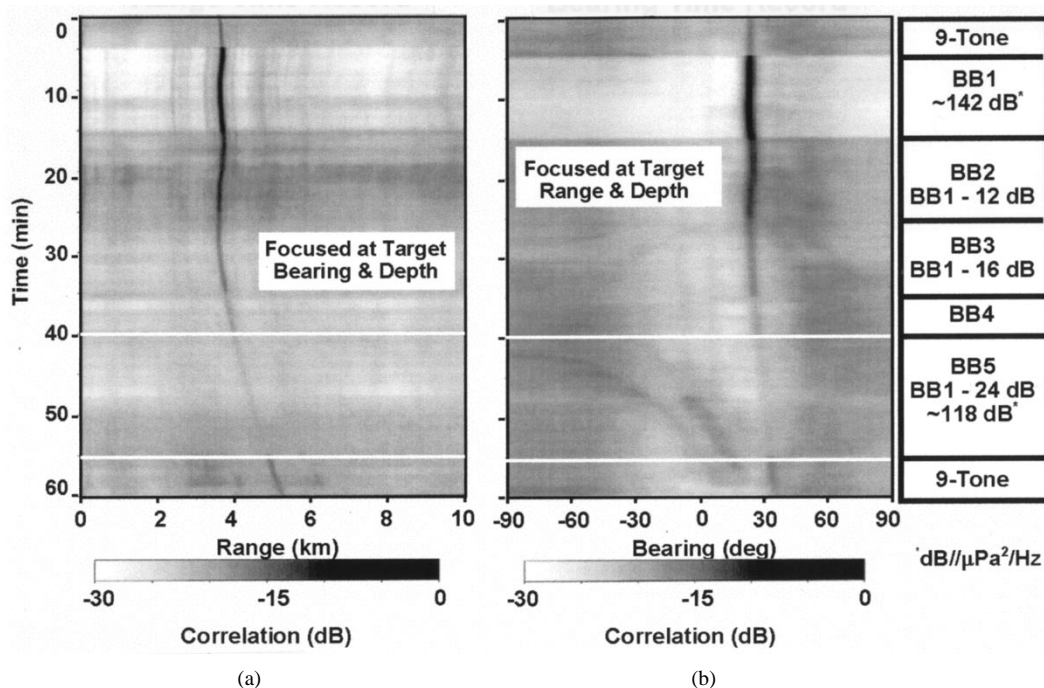


Fig. 3. Correlation (a) RTR and (b) BTR for TLA, event S48. MVDR MFP with  $WNG = -3$  dB using range-independent normal-mode replicas and frequency averaged over 100–250 Hz. The table at the far right summarizes the signals transmitted during the event. The horizontal lines at 40 and 55 min indicate the beginning and end, respectively, of the 118-dB level signal BB5.

for classification and clutter rejection. The event is described in Section II.

The TLA was initially processed to determine the source track and array tilt. The 9-tone comb signals at the beginning and end of the event were processed with broad-band linear MFP [see (2), (13), and (10)]. The frequency average was taken over the nine frequencies of the multitone signal. The output was searched in source position ( $\mathbf{r}$  and in array tilt ( $\alpha$ ) to bound the track of the source signal and to determine the array tilt that would be used for the rest of the processing ( $\alpha = 47^\circ$ ). During the broad-band signals (BB1 through BB4), the search for the source track  $\mathbf{r}(\mathbf{t})$  was accomplished with linear MFP over the 100–250-Hz band, iteratively refining the track maximizing the correlation. Since an inconsistent track was obtained with linear MFP during the period of the weakest signal (BB5), adaptive MFP [see (2), (14), (16), and (10) with  $WNG = -3$  dB] was used to obtain  $\mathbf{r}(\mathbf{t})$  during this time. This final track was used to generate the displays for the rest of the processing.

The use of *a priori* knowledge is consistent with the objectives of the analysis, which were to determine if the low-level signal was detectable. Solving the problem of searching the large range, depth, bearing, and time space at a low SNR is not addressed here, but is a critical issue for the application of MFP to passive detection systems.

#### A. Correlation Displays

Using the source track, broad-band adaptive MFP [see (2), (14), (10), (16)] with  $WNG = -3$  dB was performed on the 1-h data set to generate two types of display formats, shown in Fig. 3. The narrow-band correlation was calculated at each frequency and averaged over 150-Hz bandwidth from 100 to 250 Hz.

The bearing-time record (BTR) correlation surface is generated by focusing at the source range and depth as they change with time. A gray-scale map of output correlation [(10)] is plotted versus time and the assumed bearing of the replica steering vector. The bearing is calculated relative to TLA broad-side with increasing bearing in the easterly direction toward shore [see Fig. 1(a)]. The bearing is plotted only between  $-90^\circ$  and  $+90^\circ$  because of the inherent left/right ambiguity of the TLA and range-independent normal mode replicas. The output correlation scale in decibels is shown at the bottom of the BTR with 0 dB corresponding to perfect correlation. This plot is similar to the BTR generated with plane-wave beamforming of horizontal arrays.

The range time record (RTR) correlation surface is generated by focusing at the source bearing and depth as they change with time. The grayscale map representing the output correlation is shown plotted versus time and the assumed range. The range is calculated relative to the position of the bottom TLA hydrophone and plotted from 0 to 10 km. The RTR illustrates the range resolution of MFP and has the most contrast for the detection of weak signals.

The depth-time record, generated by focusing at the source range and bearing, is not used in this paper because it is not as good as comparing RTR plots at different depths.

As described in Table II, the source level was changed during the event. The source levels for the various time periods are shown on the right of Fig. 3. The signal can be seen most clearly on the RTR, starting at a range of  $\sim 4$  km and drifting to a range of 5.2 km as the source ship drifted away from FLIP. The range of the detection on the display is slightly larger than the true range because of localization error caused by the depth mismatch of the normal mode replicas [14] (see Section III-C). The

signal is also seen on the BTR at  $\theta = +30^\circ$  bearing and drifting slightly toward endfire east.

The changes in source level can be seen on the displays with the highest level most clearly visible. The horizontal white lines denote the beginning and end of the weakest (BB5) signal transmission. While the dynamic range of the correlation output washes out the displays, the source is seen on both the RTR and BTR displays throughout the event.

Several features of Fig. 3 can be explained by recalling from the discussion of (12) that the correlation output, when no signal is in the search cell, is the ANG. The white regions in the RTR and BTR during the transmission of the high-level signal (BB1) correspond to  $\text{ANG} < -30$  dB. The low noise gain in the ranges and bearings away from the source results from the rejection of the source's sidelobe energy by the array with adaptive MFP. Some residual source sidelobes can be seen in the RTR as vertical stripes while the source is at high signal level.

The correlation BTR on the right illustrates the directional nature of the noise in the range/depth/bearing resolution cell. High noise ( $\text{ANG} \approx -10$  dB) is measured in the upslope direction ( $\theta \geq +60^\circ$ ) toward San Diego Harbor which also corresponds to the endfire direction of the TLA where the azimuthal beamwidth is wide. Fig. 1 shows that several ships also passed through these directions. Low noise ( $\text{ANG} < -20$  dB) is seen for north/south bearings which are pointed away from the harbor and correspond to TLA broadside where the azimuthal beamwidth is narrow. The array noise gain is approximately  $-20$  dB in the vicinity of the source during the first half of the BB5 signal. The time period between 41 and 46 min where the received level is low and noise in the vicinity of the source is most stationary will be used later to compare the array performance with predictions. (Recall from the discussion with (22) that the covariance average underestimates the noise and ANG by approximately 3 dB. Thus, the true ANG in the vicinity of the source is near  $-17$  dB.) Later analysis will show that the signal excess decreases during the time period between 46 and 56 min as the region around the source becomes more noisy.

Some interference can be seen in the correlation BTR during the time of the BB5 signal starting at  $-90$  degrees (to the east) and crossing TLA broadside just prior to the end of the BB5 signal transmission. These two interference tracks are attributed to residual sidelobes of the surface ship just west of FLIP seen on Fig. 1. While the BTR is focused at the range and depth of the drifting source, the interference is still seen. This illustrates that, while gain is achieved against interfering surface ships, their bearings tend to be noisy at all ranges and depths. Note that no evidence of the surface ship interference is seen on the RTR which is focused at different bearings.

### B. Detection Displays

While the correlation displays give information about noise directionality, the low-level BB5 signal is difficult to see. In order to reduce the dynamic range in the display and to enhance the visibility of the signal, the detection displays shown in Fig. 4

are used. For each display, a detection level (DL) is obtained by estimating the local output SNR

$$\text{DL}(\mathbf{r}, t) = 10 \log \left( \frac{C(\mathbf{r}, t)}{\widehat{C}_n(\mathbf{r}, t)} - 1 \right) \quad (23)$$

where  $C(\mathbf{r}, t)$  is the correlation level at position  $\mathbf{r}$  and  $\widehat{C}_n(\mathbf{r}, t)$  is an estimate of the correlation levels in the vicinity of the search cell at position  $\mathbf{r}$ . When the cell contains a source,  $C(\mathbf{r}, t)$  is proportional to the signal power  $P_s$  plus the noise power  $P_n$  in the cell while  $\widehat{C}_n(\mathbf{r}, t)$  is an estimate of  $P_n$ . An estimate of the output SNR is obtained by subtracting 1 from the ratio.

$$\frac{P_s}{P_n} = \frac{P_s + P_n}{P_n} - 1 \approx \frac{C(\mathbf{r}, t)}{\widehat{C}_n(\mathbf{r}, t)} - 1. \quad (24)$$

For the purposes of this paper, the RTR and BTR displays were treated independently with the local noise estimated separately for each surface. Future work should examine the estimation of the local noise level as an average of the noise in the volume surrounding  $\mathbf{r}$ .

The range detection level (RDL) used for the RTR is calculated as

$$\text{RDL}(r, t) = 10 \log \left( \frac{C(r, t)}{\widehat{C}_{\text{Med}}(r, t)} - 1 \right) \quad (25)$$

where  $\widehat{C}_{\text{Med}}(r, t)$  is the median of the correlations within  $\pm 375$  m ( $\sim \pm 2$  resolution cells) of the range  $r$ . Similarly, the bearing detection level (BDL) is calculated as

$$\text{BDL}(\theta, t) = 10 \log \left( \frac{C(\theta, t)}{\widehat{C}_{\text{Med}}(\theta, t)} - 1 \right) \quad (26)$$

where  $\widehat{C}_{\text{Med}}(\theta, t)$  is the median of the correlations within  $\pm 3^\circ$  ( $\sim \pm 1$  resolution cells) of the bearing  $\theta$ . The range of the medians were chosen empirically to maximize the output signal excess which is discussed in the last technical section of this paper. When the argument of the logarithm was negative, the value was set to  $10^{-5}$ . The output, shown in Fig. 4, is plotted using a grayscale showing detection level (OSNR) values between  $-20$  and  $0$  dB. The high-level BB1 and BB2 signals which have  $\text{OSNR} > 0$  dB are truncated at  $0$  dB.

This process whitens the background noise and is similar to noise estimation and removal processes used for the detection of narrow-band lines in spectrograms [24, pp. 146–148]. Note also that the correlation output SNR (OSNR) is equal to the power OSNR because the normalization used in the correlation calculation (5) is independent of the search space parameters.

Fig. 4 shows the detection RTR and BTR displays for event S48, corresponding to the correlation records shown in Fig. 3. The horizontal lines denote the beginning and end of the weakest (BB5) signal transmission. The source is clearly detected between ranges between 4 and 5 km throughout the BB5 time period on the RTR. The residual sidelobes can be seen during the

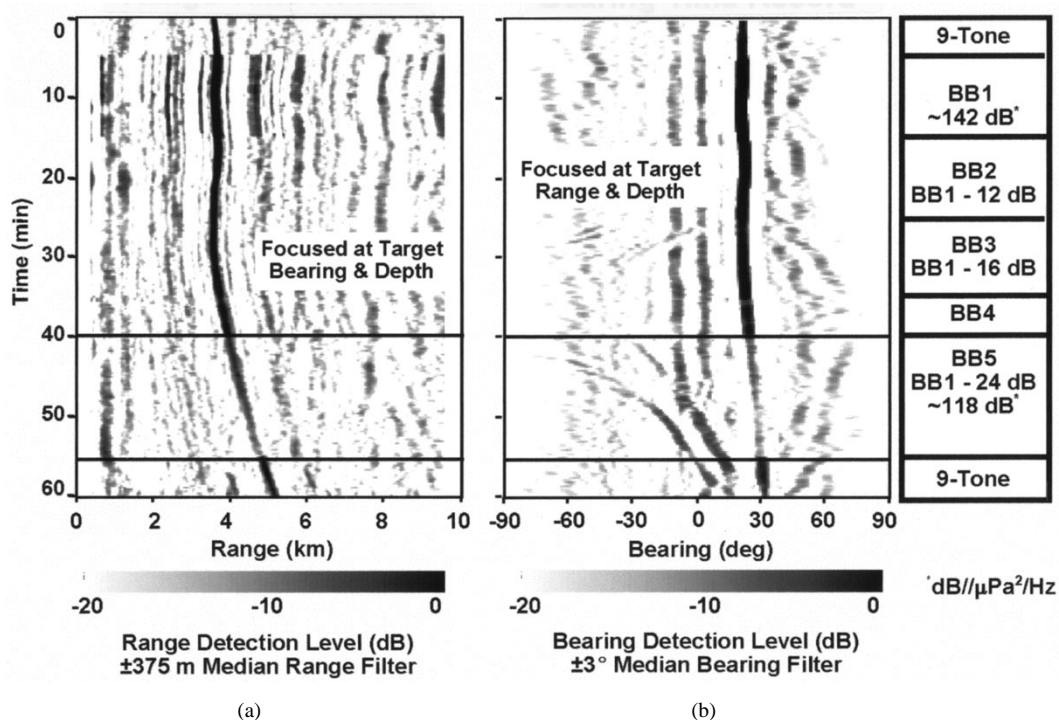


Fig. 4. Detection (a) RTR and (b) BTR for the TLA, event S48, corresponding to Fig. 3. Detection levels (OSNR estimates) are plotted on a grayscale between  $-20$  and  $0$  dB.

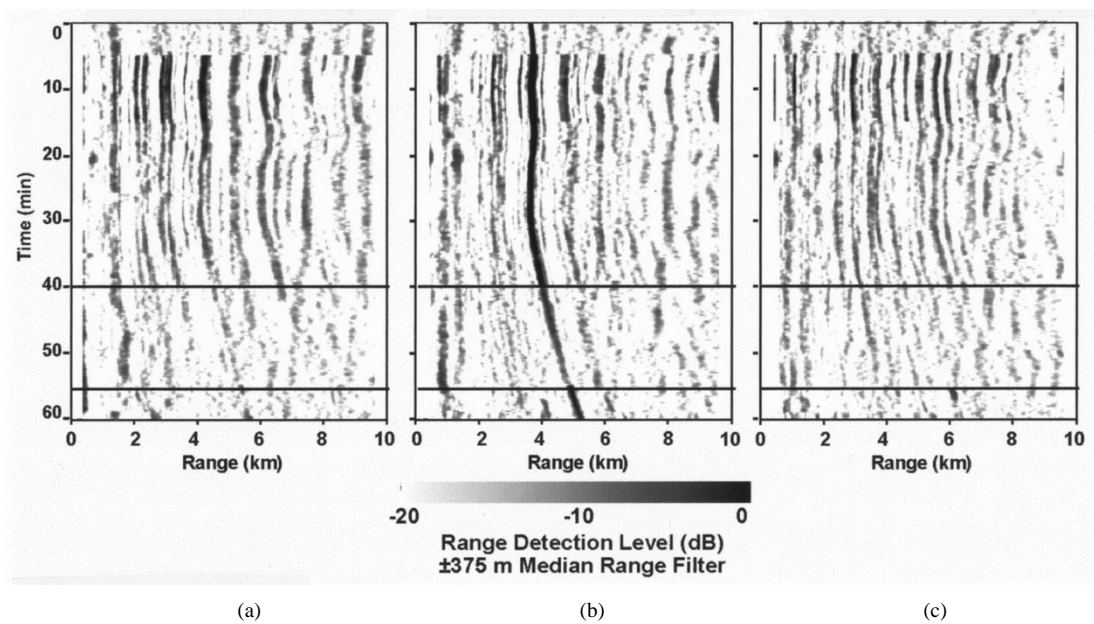


Fig. 5. TLA detection RTR's focused at depths of (a) 30, (b) 56, and (c) 90 m following the target bearing, for event S48, corresponding to Fig. 3. Detection levels (OSNR estimates) are plotted on a grayscale between  $-20$  and  $0$  dB.

transmission of signal BB1. During the time that BB5 was transmitted, the background is much smoother with few false tracks. The BTR detection display does not show the signal ( $\sim +30^\circ$  bearing) as strongly as the RTR does.

Two other detections with changing bearing are seen on the BTR starting at the beginning of the BB5 signal and continuing to the end of the record. The signals are changing bearing starting around endfire west ( $\sim -90^\circ$ ) and ending slightly east of broadside. These two detections are attributed to residual side-

lobes of the surface ship just west of FLIP seen on Fig. 1. The interfering signal is not observed in the RTR which is focused on the changing bearing of the source.

### C. Depth Resolution

The three detection RTR displays shown in Fig. 5 illustrate MFP depth resolution of weak signals. Each display is focused at the bearing that moves with the source and at different fixed search depths of 30, 56, and 90 m. While the source track is

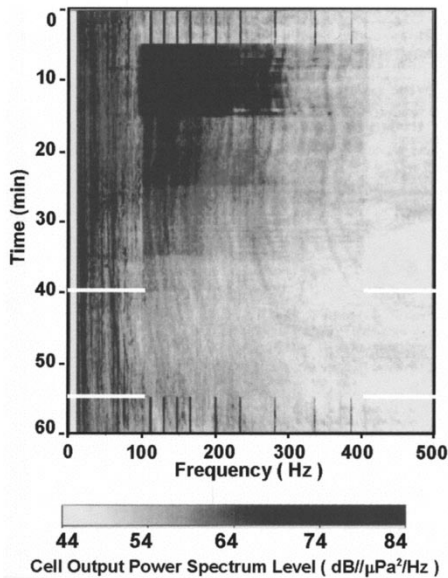


Fig. 6. Track cell spectrogram for the TLA, event S48, corresponding to Fig. 3.

clearly seen during the BB5 signal on the RTR focused at a 56-m depth, it is not seen on the RTR's focused below and above the source. The depth resolution for the water depth of the SWellEx experiment area is  $\sim 15$  m [7].

#### D. Track Cell Spectrogram

Once the source is detected and the range, depth, and bearing track  $\mathbf{r}_T(t)$  are measured, the processor can be programmed to focus on a resolution cell following the source track. The cell output power spectrum level

$$\text{COPSL} = 10 \log P_o(f, \mathbf{r}_T(t), t) \quad (27)$$

from (4) is plotted in Fig. 6 to form a track cell spectrogram. It illustrates all of the signals transmitted by the source during event S48. The 9-tone comb signal is seen in the first and last 5-min segments of the hour. The broad-band signals are seen in the 100-400-Hz band. The programmed changes in source level are also seen. During the time that the BB5 signal was transmitted, the track cell spectrogram shows no particular signal frequency that exceeds the noise level. This illustrates that the detection obtained would not have been obtained without integrating the output over frequency.

Multipath interference fringes are seen on the beamformer output spectrum. One might expect that these fringes should not be visible at the output of a matched-field beamformer since this beamformer combines the interfering multipaths. Fig. 7 shows the results of simulations that illustrate that the interference fringes result from incomplete recombination of the interfering multipaths because the array does not fully fill the water column. The simulation uses a flat spectrum signal between 100 and 400 Hz varying in level and following the track and depth of the source as in event S48. Range-independent replicas and noise-free data are calculated using conditions identical to those used in Fig. 6. A VLA and linear MFP are used for simplicity and to focus the results on the multipath interference effects. Fig. 7(a) shows the predicted spectrogram

for a single hydrophone at the center water column. Fig. 7(b) shows the track cell spectrogram for a 22-element VLA with the same vertical aperture as the TLA. Note that the spectrogram shows interference fringes similar to the real data spectrogram (Fig. 6). These fringes are not seen in Fig. 7(c), which shows the predicted spectrogram for a 54-element VLA that spans the 200-m water column.

## V. ARRAY AND PROCESSING COMPARISONS

### A. Adaptive MFP Using Arrays with Vertical Aperture

The results discussed above were obtained with the TLA and adaptive MFP (MVDR with WNG =  $-3$  dB) and represent the best results obtained for event S48. This section briefly compares the detection performance of the co-located TLA and VLA arrays with linear and adaptive processing. Fig. 8 shows detection RTR's for the four combinations of the TLA and VLA arrays with linear and adaptive processing. The RTR's are displayed best (left, TLA with MVDR) to worst (right, VLA with linear processing) based on signal excess measurements described in the next section.

The TLA-MVDR result is clearly the best with the highest SNR. The VLA results show a short range interference at the beginning of the BB5 period. The interference is rejected by the azimuthal resolution of the TLA which is tracking the drifting source in azimuth. The same interference is seen in the TLA BTR shown in Figs. 3 and 4.

The TLA results show a broad vertical stripe at short range. The TLA-MVDR result appears to have some faint false tracks which follow the source track at slightly longer range. These are attributed to residual range sidelobes of the source, similar to those seen for the strongest source levels.

In order to make the comparison quantitative, the output SNR was measured with the following procedure. For each time in the detection display, the range of the source and the peak OSNR (25) were chosen from the TLA-MVDR detection RTR as the highest peak in the display between 0.4 and 9.6 km. Peak values for the other array-processing combinations were chosen as the peaks picked within  $\pm 100$  m ( $\pm 1/2$  resolution cell) of the TLA-MVDR range. (The VLA and TLA were approximately 40 m apart with the source approximately broadside to the baseline between the arrays.) Fig. 9 shows this peak OSNR for the four combinations of arrays and processing for the time periods BB3 through BB5. Signals with negative OSNR are visible because the large time-bandwidth ( $TW = 4,500$ ) averaging smoothed the background noise.

Looking at the time during the transmission of BB5 starting at 40 min, the TLA-MVDR combination has the highest OSNR at  $-3$  dB, approximately 5 dB above the TLA-linear and VLA-MVDR results which are comparable. The VLA-linear result is another 5 dB down and is barely visible during the entire BB5 period. These results agree with the ordering of Fig. 8 and remain consistent for the higher SNR signal periods of BB3 and BB4. Between 45 and 55 min, the OSNR drops as a result of the rise in the background noise level seen in the BTR of Fig. 3.

Note that the times when the signal level was changed from BB3 to BB4 and then to BB5 can be seen and that the OSNR

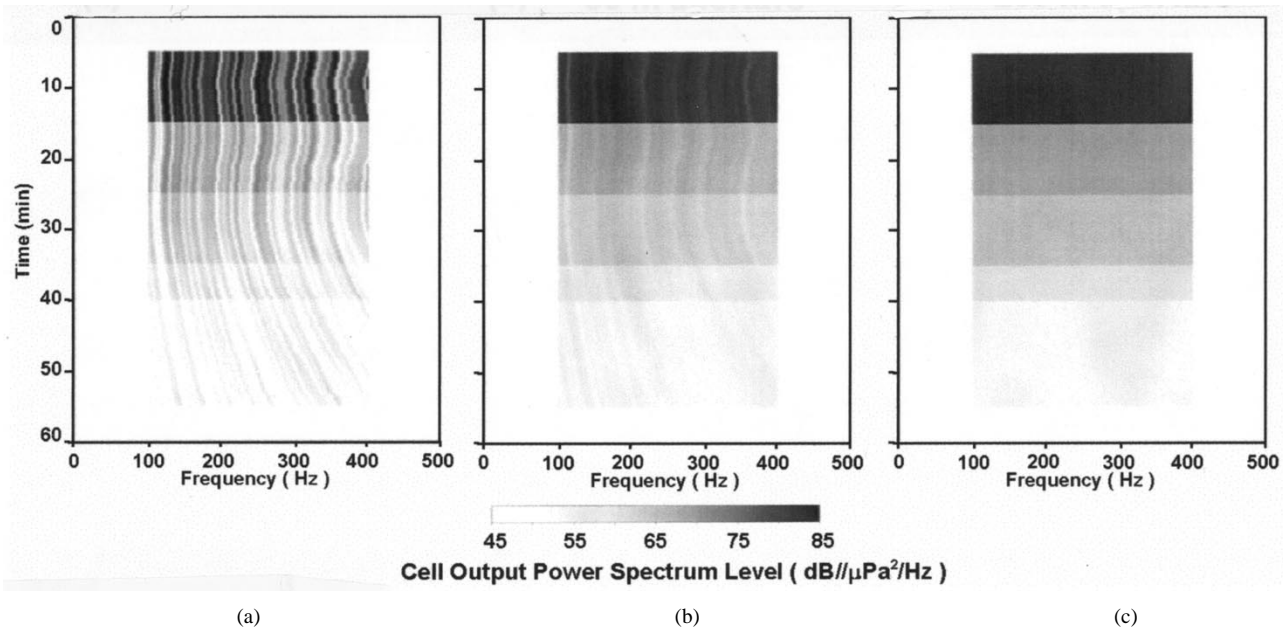


Fig. 7. Simulated track cell spectrograms: (a) single element in the middle of the TLA, (b) 22-element VLA (uniformly spaced) of the same aperture and position of the water column as the TLA, and (c) 54-element VLA (uniformly spaced) spanning the entire water column.

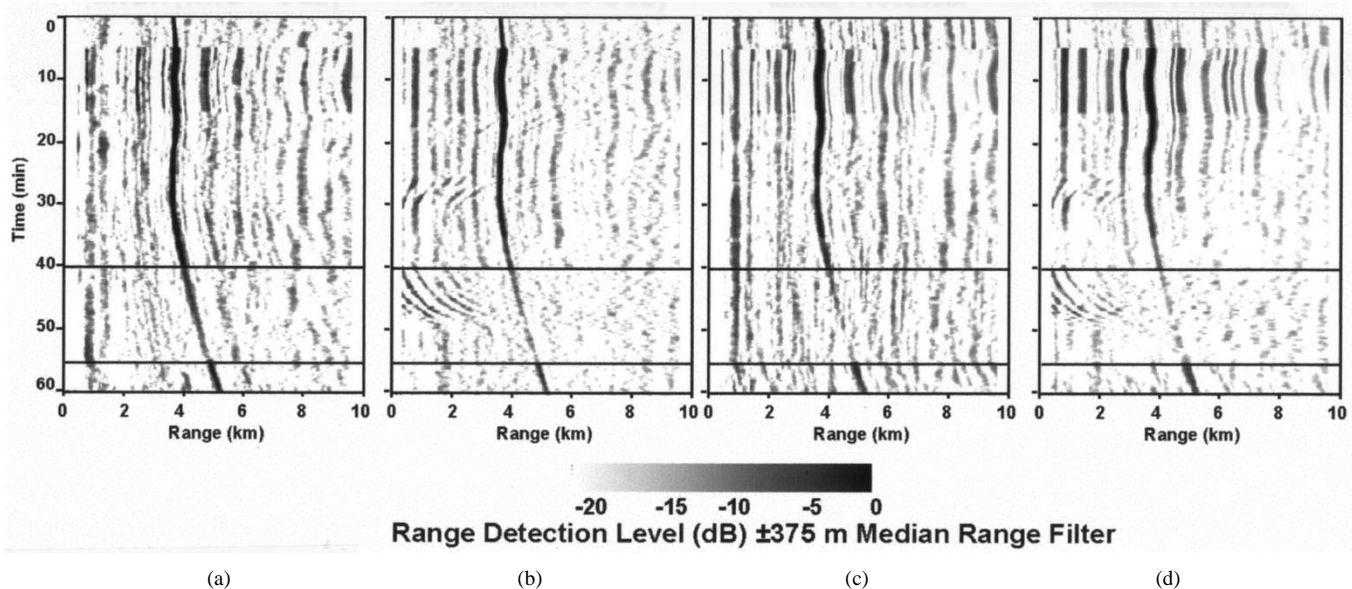


Fig. 8. Detection RTR's for processor and array comparison, ordered left to right: (a) TLA with MVDR (WNG =  $-3$  dB), (b) VLA with MVDR (WNG =  $-3$  dB), (c) TLA with linear processing, and (d) VLA with linear processing. All results are focused at the depth of the target. The TLA results follow the target bearing. Event S48 corresponds to Fig. 3. Detection levels (OSNR estimates) are plotted on a grayscale between  $-20$  and  $0$  dB.

changes by the  $\sim 4$  dB that the input SNR was changed. This is evidence that the source signal level was the intended 24 dB below the level of BB1. The 4-dB change was not seen at the highest signal levels because, with mismatch, the MVDR process is not linear, resulting in greater ASGD at higher SNR's [6], [3].

### B. Focused PWB Using an HLA

The clutter reduction resulting from the combination of azimuthal and depth resolution can be appreciated by looking at the adaptive focused plane-wave beamforming (PWB) output from the AODS-N HLA with processing parameters nearly

identical to those used with MFP and the TLA. AODS-N, shown in Fig. 1(a), was deployed on the bottom in a 213-m water depth, 1.5 km south of FLIP. The 28 elements of the array were deployed in two aperiodic subarrays over a 240-m aperture aligned  $36^\circ$  from north. The array was in a slight "V" shape with a 15-m total displacement from a straight line toward the northwest.

The array was processed with adaptive focused PWB with the AODS-N parameters listed in Table V. The replica fields (17) were calculated using a curved wavefront model focused at the 2-km range of the source from AODS-N. The correlation and detection BTR's are shown in Fig. 10. The BDL was calculated using (26), where the median was taken over  $\pm 3^\circ$  ( $\sim \pm 1$

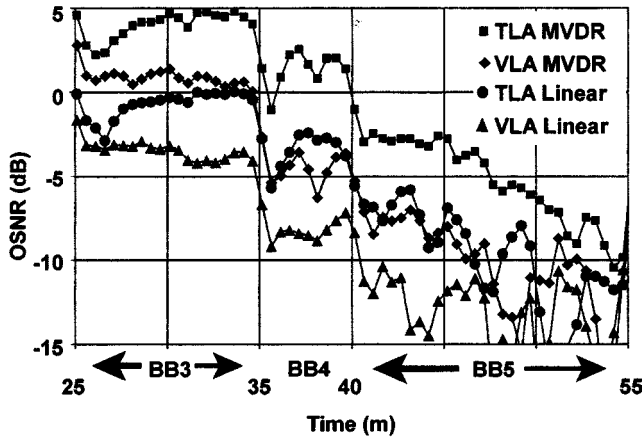


Fig. 9. Output SNR comparisons. TLA with MVDR (WNG =  $-3$  dB), VLA with MVDR (WNG =  $-3$  dB), TLA with linear processing, and VLA with linear processing.

resolution cells). The bearings are plotted as azimuth relative to north for  $360^\circ$  with endfire and broadside directions labeled on the correlation BTR. The source is the strong line between broadside and endfire south ending at  $145^\circ$  bearing. The fainter line to the right ending at  $280^\circ$  is the blurred combination of the two backlobes of the source track resulting from the “V”-shaped array.

The strong surface interference which is to the right of endfire south starting at 25 min and progressing past  $360^\circ$  toward endfire north is the track of the surface ship seen to the west of FLIP on Fig. 1(a). The dual backlobes of this interference are particularly evident to the left of endfire south in Fig. 10. The bearing track of the sidelobe detection seen in the MFP BTR’s in Figs. 3 and 4 is consistent with the track of this ship. The times also correspond with the sidelobe interferences seen on the VLA RTR’s in Fig. 8.

The several narrow interfering tracks seen ending around  $60^\circ$  are the northbound ships seen shoreward of FLIP in Fig. 1. No evidence of these ships is seen on the MFP RTR and BTR displays.

The directional nature of the ambient noise field is not as evident on the correlation BTR as with the TLA (Fig. 3) because the broadside narrow beams are pointing in the high noise direction toward San Diego Harbor. The fatter endfire beams are pointing in the quiet directions north and south. Thus, the AODS-N orientation results in a more uniform noise background.

The drifting source is detectable between broadside and endfire south with SNR’s greater than or equal to that obtained with the TLA. The higher SNR is expected given the larger horizontal aperture, the slightly larger number of elements, the shorter range, and the possibility that the tow ship contributes to the detection of the low-level source. A quantitative comparison is not made because of the inability to estimate all of these factors.

Several other surface targets are also detected on the AODS-N array. The presence of these interferences clutters the BTR, complicating the detection and classification of the submerged source.

## VI. QUANTITATIVE MEASURES OF MFP DETECTION PERFORMANCE

In order to put the processing results into perspective, we use the sonar equation to examine the detectability of the BB-5 signal in event S48 [9, p. 379]. The signal excess (SE) is given by the difference between the output SNR and the detection threshold (DT)

$$SE(BB5) = OSNR - DT = ISNR(BB5) + AG - DT \quad (28)$$

where  $ISNR(BB5)$  is the input SNR averaged over the processing band and the array elements and AG is the array gain

$$AG = OSNR - ISNR(BB5). \quad (29)$$

AG is also related to ASGD and ANG [discussed in (11) and (12)] as

$$AG = -ANG - ASGD. \quad (30)$$

AG and DT are the quantitative measures of the detection performance examined here for the array and processing combinations shown in Fig. 8.

### A. Output SNR and Array Gain

This section examines the AG achieved during the first 5 min (minutes 41–46) of the duration of the BB5 signal while the OSNR for the TLA was fairly constant at  $-3$  dB (see Fig. 9). To measure the AG, we need to estimate the input SNR (ISNR). The measured AG will be compared with a calculated approximation of the AG and the directivity index of the arrays.

The signal transmitted during event S48 is described in Table II. The received spectrogram, averaged over the 22 elements used in the processing of the TLA, is shown in Fig. 2. The 9-tone comb and BB1 signals are visible. The time period for the transmission of the BB5 signal is highlighted between the horizontal white lines.

Fig. 11(a) shows the time- and element-averaged input received power spectral levels  $IRSL(BB1)$  and  $IRSL(BB5)$ , measured on the TLA during minutes 6–11 (signal BB1) and during minutes 41–46 (signal BB5), respectively. The shaded area designates the processing band (100–250 Hz). Since  $IRSL(BB1)$  in the band of BB1 is 5–10 dB above the noise level just outside of the band, it is a good approximation of the level of the BB1 signal only. The input received source spectral level of signal BB5,  $IRSSL(BB5)$ , is estimated from  $IRSL(BB1)$  by

$$IRSSL(BB5) = IRSL(BB1) - \Delta + \delta TL \quad (31)$$

where  $\Delta$  ( $= 24$  dB for BB5) is the change made in source level from signal BB1, and  $\delta TL$  ( $= -1.25$  dB for BB5) is the change in transmission loss resulting from source drift.  $IRSSL(BB5)$  is also plotted in Fig. 11(a).

As a check on the validity of (31), the time-averaged track cell output power spectral level (COPSL) from (4) and Fig. 6 is also plotted. COPSL, which includes both signal and noise power, is below the estimate of  $IRSSL$  because of the 1-dB

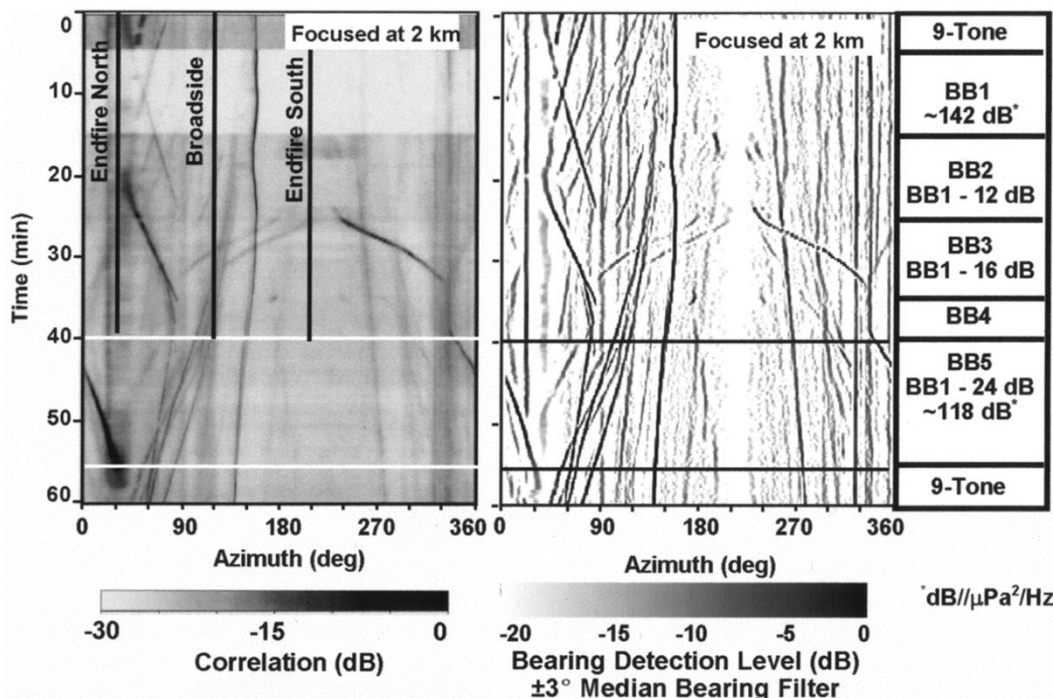


Fig. 10. Correlation and detection bearing time records from AODS-N HLA, MVDR with WNG =  $-3$  dB using PWB replicas focused at 2 km and frequency averaged over 100–250 Hz. The endfire and broadside directions are labeled on the correlation BTR.

ASGD (Table IV) and the 3-dB underestimation of the source level from inadequate CSM averaging (22).

Since  $IRSSL(BB5)$  is  $\sim 20$  dB below  $IRSL(BB5)$ , the latter measured spectrum is a good approximation of the input noise level during signal BB5

$$IRSL(BB5) \approx INL(BB5). \quad (32)$$

The ISNR spectrum is the difference between  $IRSSL(BB5)$  and  $INL(BB5)$

$$ISNR(BB5) = IRSSL(BB5) - INL(BB5) \quad (33)$$

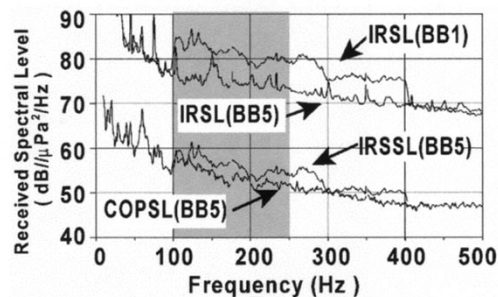
which is plotted in Fig. 11(b). The logarithm of the average input SNR over the processing band  $ISNR$  was  $-18.5$  dB.

Going back to Fig. 9 and (25), the OSNR for TLA-MVDR averaged over the processing band and over the 41–46-min duration of the time averaging  $\overline{OSNR(BB5)}$  was  $-3.0$  dB. The measured AG is the difference between  $\overline{OSNR(BB5)}$  and  $ISNR(BB5)$

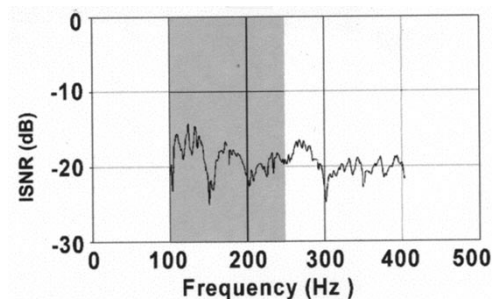
$$AG_M = \overline{OSNR(BB5)} - ISNR(BB5) \quad (34)$$

which gives an AG of  $+15.5$  dB for a TLA with MVDR processing. This number is consistent with the ANG estimate of  $-17$  dB obtained from the correlation display in Fig. 3 since ANG does not include the  $\sim 1$  dB of ASGD (see Table IV).

Similar calculations were done for the other array and processing combinations shown in Figs. 8 and 9. The results are summarized in the first row of Table VI. It should be noted that the AG for the TLA depends on the steering azimuth and the ambient noise field. Referring to Fig. 3, the source was on a quiet azimuth during the time that the AG was measured. The AG will vary with azimuth with the same dependence as the ANG [(12)].



(a)



(b)

Fig. 11. (a) Time-averaged spectra for event S48 obtained from a spectrogram are shown (Fig. 2).  $IRSL(BB1)$  (averaged from 6 to 11 min) is a measurement of the input received signal level of the BB1 signal.  $IRSL(BB5)$  (averaged from 41 to 46 min) is an estimate of the noise level measured during the transmission of the BB5 signal.  $IRSSL(BB5)$  was obtained by subtracting  $25\frac{1}{4}$  dB from the  $IRSL(BB1)$  trace. It is an estimate of the received level of the BB5 signal.  $COPSL(BB5)$  is the time-averaged track  $COPSL$  focused at the target and obtained from the track cell spectrogram (see Fig. 6). (b) Estimated ISNR spectrum for a TLA averaged over the time period between 41 and 46 min in event S48 of SWellEX-96. The shaded area represents the 100–250-Hz band of the processing.

TABLE VI  
PERFORMANCE MEASUREMENTS FOR THE BB5 SIGNAL FOR THE TIME PERIOD 41–46 MIN

	TLA-MVDR	VLA-MVDR	TLA-Linear	VLA-Linear
Measured Array Gain (dB)	15.5	11.1	10.4	6.3
Predicted Array Gain (dB)	12.5	11.2	12.5	11.2
Directivity Index (dB)	13.2	13.1	13.2	13.1
Marking Level ML 5	-9.7	-11.2	-9.6	-12.6
Detection Index	52	26	54	14
Signal Excess (dB)	7	4	3	1

AG predictions are awkward to discuss in a generic way because it depends in complicated ways on array aperture, the number of elements, and the directionality of the noise field, all of which vary with frequency. It is often predicted as

$$AG_P(f) = 10 \log(N(f)) \quad (35)$$

where  $N(f)$  is the number of independent samples. We assume that noise samples separated vertically by one wavelength and horizontally by  $1/2$  wavelength are independent [27, pp. 84–86 and 180] so that the number of independent samples for vertical and horizontal arrays are

$$N_V = \begin{cases} \frac{L_V f}{c}, & N_e > \frac{L_V f}{c} \\ N_e, & \text{otherwise} \end{cases}$$

and

$$N_H = \begin{cases} \frac{2L_H f}{c}, & N_e > \frac{2L_H f}{c} \\ N_e, & \text{otherwise} \end{cases} \quad (36)$$

respectively.  $L_V = 118$  m is the length of the VLA,  $L_H = 83$  m is the horizontal aperture of the TLA, and  $c$  is the speed of sound. This method of predicting AG takes into account the vertical anisotropy of the noise but neglects horizontal noise directionality. The predicted AG, obtained by averaging (35) over the processing band, is shown in the second row of Table VI. The third row lists the directivity index ( $DI$ ), which is the AG that would be achieved in an isotropic noise field.  $DI$  is calculated as the frequency average of

$$DI(f) = 10 \log(N(f)) \quad (37)$$

where  $N(f)$  is

$$N(f) = \begin{cases} \frac{2L_A f}{c}, & N_e > \frac{2L_A f}{c} \\ N_e, & \text{otherwise} \end{cases} \quad (38)$$

and  $L_A = 118$  m is the length of the arrays.

The measured AG for the TLA with MVDR was 2 dB in excess of  $DI$  and 3 dB in excess of  $AG_P$ . It is 4 dB better than the next highest combination and 9 dB better than the VLA with linear processing.

### B. Detection Threshold and Signal Excess

The detection threshold is a measure of signal detectability in a noise background. For broad-band signals, it is expressed as [9, pp. 428–433]

$$DT = 5 \log\left(\frac{d}{TW}\right) \quad (39)$$

where  $T$  is the integration time and  $W$  is the processing bandwidth. The detection index  $d$  is a parameter of receiver operator characteristic curves and is defined as the SNR at the detector required to achieve a given probability of detection  $P_d$  and probability of false alarm  $P_{fa}$  for a signal with  $TW = 1$ . The value of  $d$  (and  $DT$ ) assumed in making predictions depends not only on the chosen values of  $P_d$  and  $P_{fa}$ , but also on the statistics of the noise in the search space. Predictions for Gaussian statistics are presented in many books [9, pp. 428–433], [30].

For the purposes of comparing detection performance, we select a threshold for each array-processor combination shown in Fig. 9 during the time of the BB5 signal using the following procedure.

- The range detection level [(25)] samples at all ranges between  $375 \text{ m} < r < 9,625 \text{ m}$  for the times between  $41 < t < 54 \text{ min}$  are concatenated and sorted.
- The level exceeded by 5% of the samples is chosen as a threshold which is called the threshold marking level  $ML_x$  for  $x = 5\%$  marking rate.
- The RTR's are replotted such that any sample exceeding the threshold is black and the other samples are white.

The resulting plots, called thresholded RTR's, are shown in Fig. 12. Signals which exceed the marking levels have OSNR's greater than the marking level

$$\text{OSNR} > \text{ML}_5, \quad (40)$$

The marking level can be considered an empirical detection threshold. When it is obtained in the same way for each array-processing combination,  $ML_x$  is a measure of the smoothness of the background in which the detection is being made. (This interpretation is not meaningful for detections in a background dominated by the sidelobes of a strong interfering signal as during the transmission of signal BB1.) Like the detection threshold, it is low for a smooth background and higher for a rough background.  $ML_5$  are listed in Fig. 12 and in Table VI along with the associated detection index  $d$ , which

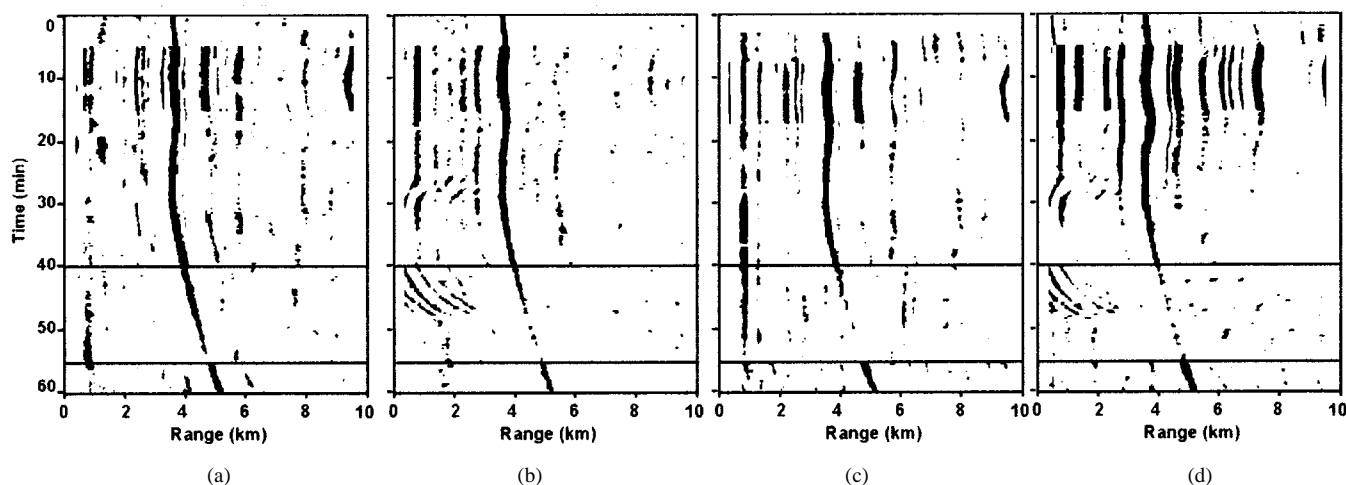


Fig. 12. Thresholded RTR's. The threshold ( $ML_5$ ) was chosen for each array and processing combination to give a marking rate of 5% for the time period between 41 and 54 min. (a) TLA MVDR.  $ML_5 = -9.7$  dB. (b) VLA MVDR.  $ML_5 = -11.2$  dB. (c) TLA linear.  $ML_5 = -9.6$  dB. (d) VLA linear.  $ML_5 = -12.6$  dB.

was obtained from (39) by setting  $DT = ML_5$  and using  $TW = 4521$  (see Table V).

The marking rate differs from the probability of false alarm because some of the marks include the signal. Thus,  $P_{fa}$  is less than the 5% marking rate. The true  $P_{fa}$  for the TLA-MVDR combination is more like 2% while it is closer to 5% for the VLA-linear combination. The differences could have been avoided using our knowledge of the location of the signal. However, since such knowledge is not available when setting the threshold for realistic detection systems, the above method was chosen as a more realistic comparison of the array and processing systems. Note also that the  $P_{fa}$  used in this context is based upon a single 30-s scan and does not include reductions from integration along tracks.

Examination of the thresholded RTR's in Fig. 12 supports the ranking of the systems as that based on the measured AG shown in Table VI. Note, however, that the detection threshold for the VLA is considerably lower than for the TLA in spite of the interfering sidelobes in the first half of the BB5 time period. This is supported by the smoothness of the VLA detection RTR's in Fig. 8.

We compare the array and processing combinations discussed in this paper by calculating the signal excess using (28) where the detection threshold  $DT = ML_5$  for a constant marking rate is subtracted from the OSNR. The results are plotted in Fig. 13 where we see that the TLA-MVDR combination of array and processing has the largest signal excess.

## VII. SUMMARY AND CONCLUSIONS

We have presented evidence that low-level signals are detectable in a typical shallow-water noise environment with moderate shipping interference using adaptive MFP techniques applied to arrays with vertical aperture  $1/3$  to  $1/2$  the water depth. The best detection performance was obtained with the TLA with the MVDR adaptive algorithm using white noise gain constraint ( $WNG = -3$  dB). The measured array gain which exceeded the directivity index by  $\sim 3$  dB resulted primarily from the azimuthal directionality of the noise field observed with the  $4^\circ$  to  $8^\circ$  bearing resolution of the TLA. A spectrogram following the

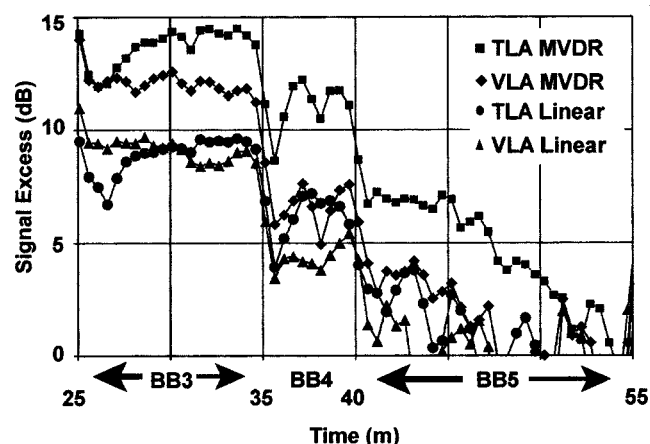


Fig. 13. Signal excess for a 5% display marking rate measured during signal BB5.

track of the source showed multipath interference effects in the MFP output for arrays with vertical aperture less than the water depth.

A quantitative comparison of the detection performance of the TLA and the VLA with both linear and MVDR processing indicated that, for this test, the TLA-MVDR combination showed the largest signal excess for low-level signals. The VLA-MVDR and TLA-linear combination were comparable and slightly better than the VLA with linear processing. In general, the VLA had less AG than the TLA, but the smoothness of the background (resulting from the inherent azimuthal averaging) allowed a lower detection threshold for the same 5% probability of display marking.

Qualitative comparison with a nearby HLA indicated that the OSNR's were comparable but that detection and classification with the HLA was complicated by the multiple surface ship interferences.

## REFERENCES

- [1] R. T. Bachman, P. W. Schey, N. O. Booth, and F. J. Ryan, "Geoacoustic data bases for matched-field processing: Preliminary results in shallow water off San Diego, California," *J. Acoust. Soc. Amer.*, vol. 99, pp. 2077-2085, 1996.

- [2] A. B. Baggeroer, W. A. Kuperman, and H. Schmidt, "Matched field processing: Source localization in correlated noise as an optimum parameter estimation problem," *J. Acoust. Soc. Amer.*, vol. 83, pp. 571–587, 1988.
- [3] A. B. Baggeroer, W. A. Kuperman, and P. N. Mihalevsky, "An overview of matched field methods in ocean acoustics," *IEEE J. Oceanic Eng.*, vol. 18, pp. 401–424, 1993.
- [4] P. A. Baxley, N. O. Booth, and W. S. Hodgkiss, "Matched-field replica model optimization and bottom property inversion in shallow water," *J. Acoust. Soc. Amer.*, vol. 107, pp. 1301–1323, 2000.
- [5] J. S. Bendat and A. G. Piersol, *Random Data Analysis and Measurement Procedures*. New York, NY: Wiley, 1986, ch. 9, pp. 291–294.
- [6] N. O. Booth and G. L. Mohnkern, "Signal-to-noise gain from adaptive matched-field beamforming of multidimensional acoustic arrays, NRaD TR 1661," Naval Command, Control and Ocean Surveillance Centre, San Diego, CA, RDT&E Div, Sept. 1994.
- [7] N. O. Booth, P. A. Baxley, J. A. Rice, P. W. Schey, W. S. Hodgkiss, G. L. D'Spain, and J. J. Murray, "Source localization with broadband matched field processing in shallow water," *IEEE J. Oceanic Eng.*, vol. 21, pp. 402–412, 1996.
- [8] H. P. Bucker, "Use of calculated sound fields and matched-field detection to locate sound sources in shallow water," *J. Acoust. Soc. Amer.*, vol. 59, pp. 368–373, 1976.
- [9] W. S. Burdic, *Underwater Acoustic Systems Analysis*. Englewood Cliffs, NJ: Prentice-Hall, 1991.
- [10] J. Capon and N. R. Goodman, "Probability distributions for estimates of the frequency-wavenumber spectrum," *Proc. IEEE*, vol. 58, pp. 1785–1786, 1970.
- [11] J. Capon and N. R. Goodman, "Erratum: Probability distributions for estimates of the frequency-wavenumber spectrum," *Proc. IEEE*, vol. 59, p. 112, 1971.
- [12] H. Cox, R. M. Zeskind, and M. M. Owen, "Robust adaptive beamforming," *IEEE Trans. Acoust., Speech Signal Processing*, vol. 35, pp. 1365–1376, 1987.
- [13] R. D. Doolittle, A. Tolstoy, and E. J. Sullivan, Editor, Guest Editors, *IEEE J. Oceanic Eng.*, vol. 18, pp. 153–205, 1993.
- [14] G. L. D'Spain, J. J. Murray, W. S. Hodgkiss, and N. O. Booth, "Mirages in shallow water matched field processing," *J. Acoust. Soc. Amer.*, vol. 105, pp. 3245–3265, 1999.
- [15] C. Eckert, Optimal rectifier systems for the detection of steady signals, Marine Physical Laboratory of Scripps Institution of Oceanography, La Jolla, CA, 1952.
- [16] P. M. Embree and B. Kimble, *C Language Algorithms for Digital Signal Processing*, NJ: Prentice Hall, 1991, ch. 1, p. 38.
- [17] R. A. Gramann, "ABF algorithms implemented at ARL:UT," Applied Research Laboratories, University of Texas, Austin, TX, ARL/UT Technical Report 92-7, May 1992.
- [18] D. E. Grant, J. H. Gross, and M. Z. Lawrence, "Cross-spectral matrix estimation effects on adaptive beamforming," *J. Acoust. Soc. Amer.*, vol. 98, pp. 517–524, 1995.
- [19] F. J. Harris, "On the use of windows for harmonic analysis with discrete Fourier transform," *Proc. IEEE*, vol. 66, pp. 51–83, 1987.
- [20] W. S. Hodgkiss, J. C. Nickles, G. L. Edmonds, R. A. Harriss, and G. L. D'Spain, "A large dynamic range vertical array of acoustic sensors," in *Full Field Inversion Methods in Ocean and Seismo-Acoustics*, O. Diachok et al., Eds, MA: Kluwer, 1995, pp. 205–210.
- [21] W. S. Hodgkiss, D. E. Ensberg, J. J. Murray, G. L. D'Spain, N. O. Booth, and P. W. Schey, "Direct measurement and matched field inversion approaches to array shape estimation," *IEEE J. Oceanic Eng.*, vol. 21, pp. 393–401, 1996.
- [22] J. P. Ianniello, "Recent developments in sonar signal processing," *IEEE Signal Processing Mag.*, vol. 15, pp. 27–40, 1998.
- [23] Z.-H. Michalopoulos and M. B. Porter, "Matched-field processing for broad-band source localization," *IEEE J. Oceanic Eng.*, vol. 21, pp. 384–392, 1996.
- [24] R. O. Nielsen, *Sonar Signal Processing*. Boston, MA: Artech House, 1991.
- [25] N. Owsley, *Array Signal Processing*, S. Haykin, Ed. Englewood Cliffs, NJ: Prentice-Hall, 1985, ch. 3.
- [26] M. B. Porter, "The KRAKEN normal mode program," SACLANT Undersea Research Centre, La Spezia, Italy, Rep. SM-245, 1991.
- [27] B. D. Steinberg, *Principles of Aperture and Array System Design*. New York, NY: Wiley, 1976.
- [28] S. Stergiopoulos and A. T. Ashley, Guest Editors, "Special issue on sonar system technology," *IEEE J. Oceanic Eng.*, vol. 18, pp. 361–582, 1993.

- [29] G. B. Smith, C. Feuillade, and D. R. DelBalzo, "Matched-field processing enhancement in a shallow-water environment by incoherent broadband averaging," *J. Acoust. Soc. Amer.*, vol. 91, pp. 1447–1445, 1992.
- [30] R. J. Urick, *Principles of Underwater Sound*, 3rd ed. New York, NY: McGraw-Hill, 1983, ch. 12, pp. 377–403.
- [31] E. K. Westwood, "Broadband matched-field source localization," *J. Acoust. Soc. Amer.*, vol. 91, pp. 2777–2789, 1992.
- [32] J. H. Wilson, S. D. Rajan, and J. M. Null, Guest Editors, "Special issue on inversion techniques and the variability of sound propagation in shallow water," *IEEE J. Oceanic Eng.*, vol. 21, pp. 321–480, 1996.



**Newell O. Booth** received the B. A. degree in physics from the University of California at Berkeley in 1962 and the Ph. D. degree in plasma physics from the University of California at Los Angeles in 1970.

He has been a Research Physicist at the Space and Naval Warfare (SPAWAR) Systems Center, San Diego, CA, and its predecessor laboratories since 1963, specializing in the exploratory development of advanced antisubmarine warfare systems. His fields of expertise include signal processing, underwater acoustics, ocean engineering, acoustic source and receive array design, performance prediction, and matched-field beamforming. On assignment at the Office of Naval Research (ONR) between 1987 and 1990, he organized and managed the High Gain Initiative, the first major research program in matched-field processing. He has since managed several matched-field processing projects under the sponsorship of the ONR and DARPA. He is currently associated with the SPAWAR Systems Center as a retired emeritus scientist.

Dr. Booth received several awards for his outstanding contributions to the field of high-resolution matched-field processing, including the IEEE Oceanic Engineering Society's 1998 Distinguished Technical Achievement Award and the 1999 SPAWAR Systems Center's Lauritzen-Bennett Award.

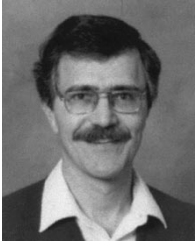


**Ahmad T. Abawi** was born on November 5, 1957, in Kabul, Afghanistan. He received the B.S. degree in electrical engineering and the B.S. degree physics from the University of California at Irvine in 1983 and 1984, respectively, and the M.S. and Ph.D. degrees in physics from the University of California at San Diego in 1988 and 1993, respectively.

From 1993 to 1995, he was a Post-Doctoral Physicist at the Marine Physical Laboratory of Scripps Institution of Oceanography, La Jolla, CA, where he worked on propagation modeling and signal processing. Between 1995 and 1997, he worked at the Arete Engineering Technologies Corporation, San Diego, CA, where his work involved sonar data analysis, signal processing, and sonar cross-section analysis. Since 1997, he has been working at the SPAWAR Systems Center, San Diego, where his current work is on array signal processing, matched-field processing, data analysis, and propagation modeling. His other research interests include scattering theory and orbital mechanics.

**Phil W. Schey** received the B.A. degree in mathematics from San Diego State University, San Diego, CA, in 1971.

Between 1976 and 1989, he specialized in acoustic data analysis and propagation modeling for the Computer Sciences Corporation. He has been a Research Scientist at Space and Naval Warfare (SPAWAR) Systems Center, San Diego, CA, and its predecessor laboratories since 1989, specializing in matched-field processing, propagation modeling, sonar system performance prediction, signal processing, and array dynamics. He is currently involved in several matched-field processing data analysis projects.



**William S. Hodgkiss** (S'68-M'75) was born in Bellefont, PA, on August 20, 1950. He received the B.S.E.E. degree from Bucknell University, Lewisburg, PA, in 1972, and the M.S. and Ph.D. degrees from Duke University, Durham, NC, in 1973 and 1975, respectively.

From 1975 to 1977, he worked with the Naval Ocean Systems Center, San Diego, CA. From 1977 to 1978, he was a Faculty Member in the Electrical Engineering Department, Bucknell University. Since 1978, he has been a Member of the Faculty of the Scripps Institution of Oceanography, La Jolla, CA, and on the staff of the Marine Physical Laboratory, University of California at San Diego. Currently he is Deputy Director, Scientific Affairs, Scripps Institution of Oceanography. His present research interests are in the areas of signal processing, propagation modeling, and environmental inversions with applications of these to underwater acoustics and electromagnetic wave propagation.